REPORT DOCUMENTATION PAGE

AFRL-SR-AR-TR-03-

0145

Public reporting burden for this collection of information is estimated to average 1 hour per response, including the time for reviewing in data needed, and completing and reviewing this collection of information. Send comments regarding this burden estimate or any other this burden to Department of Defense, Washington Headquarters Services, Directorate for Information Operations and Reports (0704-(4302. Respondents should be aware that notwithstanding any other provision of law, no person shall be subject to any penalty for faili valid OMB control number. PLEASE DO NOT RETURN YOUR FORM TO THE ABOVE ADDRESS.

1. REPORT DATE (DD-MM-YYYY) 02/28/03	2. REPORT TYPE Final Report	3. DATES COVERED (From - To) 1/15/00 – 11/30/02

4. TITLE AND SUBTITLE

Applying New Methods to Flare Prediction Using Photospheric Vector Magnetic Field Data

5a. CONTRACT NUMBER
F49620-00-C-0004

5b. GRANT NUMBER

5c. PROGRAM ELEMENT NUMBER

6. AUTHOR(S)
Dr. K.D. Leka

5d. PROJECT NUMBER

5e. TASK NUMBER

5f. WORK UNIT NUMBER

7. PERFORMING ORGANIZATION NAME(S) AND ADDRESS(ES)

NorthWest Research Associates
14508 NE 20th St.
PO Box 3027
Bellevue, WA 98009-3027

8. PERFORMING ORGANIZATION REPORT NUMBER
NWRA-CoRA-03-R253

9. SPONSORING / MONITORING AGENCY NAME(S) AND ADDRESS(ES)
Air Force Office of Scientific Research
AFOSR/PKA Attn: Major Paul Bellaire, Jr.
4015 Wilson Blvd. #713
Arlington, VA 22203-1954

10. SPONSOR/MONITOR'S ACRONYM(S)

11. SPONSOR/MONITOR'S REPORT NUMBER(S)

12. DISTRIBUTION / AVAILABILITY STATEMENT

13. SUPPLEMENTARY NOTES

14. ABSTRACT

The feasibility of using photospheric vector magnetic field data for solar flare prediction is tested using three distinct approaches. First, we examine on a case-by-case basis, the magnitude and variations of over eighty parameters (almost two hundred when both mean and slope are considered), derived from the vector magnetic field data which describe the magnetic state of the active-region photosphere. We find that when pre-event variations and levels are examined using both flare-producing and flare-quiet regions, any obvious or uniquely flare-related signatures are rare. Second, a statistical approach is used for all parameters and all seven active regions (ten flares and fourteen flare-free samples). We demonstrate that (1) combinations of parameters can be found which perfectly distinguish between flare-imminent and flare-quiet samples, but (2) that these combinations are not unique, primarily due to the small sample; still, (3) we are able to identify parameterizations of the distribution of electric current density, magnetic-field twist, and current helicity as well as neutral-line shear angle which routinely appear in well-performing discriminant functions. Third, we demonstrate an application of the Magnetic Charge Topology model to photospheric data, with which we can quantify the complexity of the coronal fields as related to flare events.

15. SUBJECT TERMS

16. SECURITY CLASSIFICATION OF:			17. LIMITATION OF ABSTRACT	18. NUMBER OF PAGES	19a. NAME OF RESPONSIBLE PERSON
a. REPORT Unclassified	**b. ABSTRACT** Unclassified	**c. THIS PAGE** Unclassified	UL	31	19b. TELEPHONE NUMBER (include area code)

Standard Form 298 (Rev. 8-98)
Prescribed by ANSI Std. 239.18

20030523 154

FINAL TASK REPORT

Instructions: Provide all information identified below for the duration of this project. List Research Objectives in bullet format. Provide Summary of Research narrative format.

Research Title: **Applying New Methods to Flare Prediction Using Photospheric Vector Magnetic Field Data**

Principal Investigator: **Dr. K. D. Leka**

Commercial Phone: **303-415-9701 x219** FAX: **303-415-9702**

Mailing Address: **NorthWest Research Associates, Colorado Research Associates Division**

3380 Mitchell Ln.

Boulder, CO 80301

E-Mail Address: **leka@cora.nwra.com**

AFOSR Program Manager: **Maj. Dr. Paul Bellaire**

Research Objectives:
- Develop and demonstrate a statistical method to inter-compare the flare-predictive capability of parameters derived from photospheric vector magnetic field data.
- Apply the "Minimum Coronal Current" algorithm (Longcope, 1996) to photospheric vector magnetic field data with the goal of quantifying the coronal magnetic complexity and its evolution as it relates to flare productivity
- Acquire and prepare vector magnetogram data to test and demonstrate the feasibility of the above methods, ensuring that the data are sufficiently quantitative and accurate as to be appropriate for this project.

Funding Summary ($K):

In House	Capital Equip. (> $5,000 each)	Subcontractor	Total
$261,456	$5,546	$69,383	$336,385

Summary of Progress: *see Attachment 1*

Leka 2002, *An Evaluation of Flare Predictors from Photospheric Magnetic Field Data I: Data, Method, and Temporal Variations,* Astrophysical Journal

LaBonte & Leka 2002, *The Imaging Vector Magnetograph at Haleakala III: Determining The Magnetic Atmosphere,* Solar Physics.

Longcope, Barnes & Leka 2002, *Coronal Topology Changes Associated with Solar Flares: an Application of the Minimum Coronal Current Analysis,* Astrophysical Journal

Barnes & Leka 2002, *An Evaluation of Flare Predictors from Photospheric Magnetic Field Data, II: Applying a Discriminant Function,* Astrophysical Journal.

Appendix A: In-house Activities

Instructions: Provide all information identified below for the duration of the research project. "Personnel" should include each scientist or engineer who contributed to the research. Publication of articles derived from the research should be listed chronologically in bibliography format. Attach reprints. List only invention disclosures derived from this specific research effort. Honors may include recognition both inside and outside the academic and Air Force science & technology (S&T) communities. Extended scientific visits may include collaboration with other research programs, both foreign and US.

Personnel:

Name	Degree	Discipline	Involvement
In House Employees			
K. D. Leka	Ph.D.	Research Scientist, P.I. 0.5 FTE (2000-2002)	
Graham Barnes	Ph.D.	Research Scientist, 1.0 FTE (2001-2002)	
Sharon Vadas	Ph.D.	Research Scientist/Programmer 0.1FTE (2000-2002)	
Subcontractors			
Dana Longcope (Montana State University)			
	Ph.D.	Professor	0.1FTE (2000-2002)
K. E. Rangarajan (Montana State University, on leave from the Indian Institute of Astrophysics).			
	Ph.D.	PostDoctoral Research Assistant 1.0FTE (2000-2001)	
Visitors			

Publications Citing this Support:

Published in Peer Reviewed Journals and Books:
Leka, K. D. and Rangarajan, K. E. 2001, *Effects of 'Seeing' on Vector Magnetograph Measurements*, Solar Physics, **203**, #2,239-254.

Published in Unreviewed Publications (proceedings, tech. reports, etc.)

Accepted/Submitted for Publication:
Leka, K. D. and Barnes, G., 2003, *Photospheric Magnetic Field Properties of Flaring vs. Flare-Quiet Active Regions I: Data, General Analysis Approach, and Sample Results*, Astrophys. J. (submitted).
Leka, K. D. and Barnes, G., 2003, *Photospheric Magnetic Field Properties of Flaring vs. Flare-Quiet Active Regions II: Applying a Discriminant Function*, Astrophys. J. (submitted).
Barnes, G., Leka, K. D. and Longcope, D. W., *Photospheric Magnetic Field Properties of Flaring vs. Flare-Quiet Active Regions III: an Application of the Magnetic Charge Topology Model*, Astrophys. J., (in preparation)

Invention Disclosures and Patents Granted: (code listing for algorithms developed: see Attachment 2)

Invited Lectures, Presentations, Talks, etc.:

Active Region Evolution with the Imaging Vector Magnetograph, (Leka & Rangarajan), presented at the 20th Sacramento Peak Summer Workshop, September, 2000

The Effect of Seeing on Vector Magnetograph Measurements of Solar Active Regions (Leka & Rangarajan), presented at the Spring AGU/2001 SPD annual meeting, Boston, May 2001.

Practical Uses of Vector Magnetic Field Data, Invited Presentation at the GOES-R Planning Meeting (Leka), Space Environment Center/NOAA, October 2001.

The Roots of Change: Solar Magnetic Structures as Drivers of Solar Variability, Invited Colloquium (Leka), U. New Hampshire, November 2001.

The Roots of Change: Understanding the Magnetic Drivers of Solar Variability, Invited Seminar (Leka), U. Hawai'i, December 2001.

Photospheric Magnetic Fields and Solar Flares I: Data and Initial Diagnostics, (Leka & Barnes), presented at the 2002 Space Weather Week, Boulder CO, April 2002.

Photospheric Magnetic Fields and Solar Flares II: Coronal Complexity and Magnetic Topology (Barnes, Leka & Longcope) presented at the 2002 Space Weather Week, Boulder CO, April 2002.

Are We There Yet?? The Drive to Understand and Predict Solar Energetic Events, Invited Colloquium (Leka), NOAA/Space Environment Center, April 2002.

Photospheric Magnetic Fields' Complexity Variations and Solar Flares (Barnes, Leka & Longcope) presented at the 2002 annual meeting of the Solar Physics Division of the American Astronomical Society, Albuquerque, NM, June 2002.

Photospheric Magnetic Fields' Complexity Variations and Solar Flares (Barnes, Leka & Longcope) presented at the Solar, Heliospheric and Interplanetary Environment (SHINE) 2002 Summer Workshop, Banff, Alberta, Canada, August 2002.

Professional Activities (editorships, conference and society committees, etc.):
The P.I. is currently serving on the National Solar Observatory User's committee. She served as an elected member for the council of the AAS/Solar Physics Division 2000-2002.

Honors Received (include lifetime honors such as Fellow, honorary doctorates, etc., stating year elected):

Extended Scientific Visits From and To Other Laboratories:
Dr. Dana Longcope visited CoRA/NWRA on at least four extended occasions during this project; his visits were annual if not more frequent.
Dr. K. D. Leka visited the U. Hawai'i/Institute for Astronomy on three occasions for collaboration and data retrieval.
Dr. Barnes traveled to Montana State University to consult with Dr. Longcope on the application of the Minimum Coronal Current Analysis in late August 2001.

Appendix B: Off-Site Contract and Grant Activities

Instructions: Provide all information identified below for the last FY only. Publication of articles derived from the research should be listed chronologically in bibliography format. Attach reprints. List only invention disclosures derived from this specific research effort.

Publications: None

Invention   **Disclosures:**

Appendix C: Technology Transitions/Transfers Detailed Listing

Performer (name, telephone, and organization)	Customer(s) (name and organization)	Research Result (scientific statement)	Application (technical benefit(s) and/or customer useB List and underline any military applications first)	Transi tioned To	Transi tioned From	Appli cation
Leka, Barnes, Longcope	(TBD)	see below	see below	(TBD)	I/A	Pc

The discriminant function analysis of observables derived from vector magnetic field data, including the results from the Minimum Coronal Current parameterizations, will be applicable by government and other agencies for evaluating the potential of the Sun to produce geo-effective energetic events. The peer-review system for the publications outlining the process need to be exploited and the algorithms need to be tested before any release is undertaken. We are planning this process, and wish to proceed given additional funding for this project.

Note: In the last three columns enter the following codes:

Transitioned From:
AFRL = L
Industry = I
Academia = A

Transitioned To:
Industry = I
Air Force 6.2 or 6.3 = AF
Other AF, DoD, or Government = O

Application:
Product (New or Improved) = Pd
Process (New or Improved) = Pc
Other Technology Benefit = O

ATTACHMENT 1: PROJECT SUMMARY

Contents

Accomplishments/New Findings:

1 Original Goals

The stated goals for this project can be summarized as the following:

1. *Develop a method to inter-compare the flare-predictive capability of parameters derived from photospheric vector magnetic field data.*

2. *Apply the "Minimum Coronal Current" algorithm [23] to photospheric vector magnetic field data with the goal of quantifying the coronal magnetic complexity as it relates to flare productivity, and*

3. *Acquire and prepare vector magnetogram data to test and demonstrate the feasibility of the above methods, ensuring that the data are sufficiently quantitative and accurate as to be appropriate for this project.*

In short, we have full-filled our commitment; as described below, in some cases the goals were hindered by unforeseen problems, yet in others our initial goal has been surpassed. In both situations, we continue our close collaboration with scientists at many institutions, including the National Center for Atmospheric Research (Drs. S. Gibson and Y. Fan), U. C. Berkeley (Dr. G. Fisher/the MURI team), Montana State U. (Drs. D. Longcope, R.C. Canfield and other MURI team members).

Below we summarize our accomplishments and new findings from this project.

2 Producing Quantitative Time-Series of Photospheric Vector Magnetic Field

A significant amount of the effort for this project has been directed to producing time-series of photospheric vector field data that are adequately characterized. Both and random uncertainties must be understood, quantified, and included such that variations observed in the time-sequence are trusted to educate us on the solar condition.

2.1 The General Data Reduction

The data used in this project are from the U. Hawai'i/Mees Solar Observatory Imaging Vector Magnetograph at Haleakalā [28, 13, 12]. Briefly, the spar-mounted IVM was designed to minimize both instrumental polarization and internal turbulence. A four-frame polarization-modulation sequence is employed, using a Fabry Perot etalon to sample 30 wavelength positions across the magnetically sensitive ($g_{eff} = 2.5$) FeI 630.25nm spectral line in under 2 minutes.

Corrections to the raw data are performed to remove spatial and polarization distortions from both the telescope system and atmospheric seeing [28, 13]. The data are then demodulated to produce Stokes spectra ($[I, Q, U, V]$) at each pixel [13]. As a final step, the spectra are binned to 256^2 1.1″ pixels. The final polarization noise (normalized by I_continuum) is of order 2×10^{-3} in these data.

To derive the magnetic flux vector from the resulting spectropolarimetric data, we employ a forward-integration scheme based upon the equations of [14, 15], which produces results comparable to a full least-squares inversion [12]. The resulting maps of the observed line-of-sight and transverse

1

magnetic components have uncertainties of order 10G (B_ℓ), 25G (B_t), with an uncertainty in the azimuthal angle of approximately 5 deg.

The 180deg ambiguity in the observed transverse component is resolved using an automated iterative procedure which minimizes the difference between the observed field and a force-free field computed using the B_z component and which additionally minimizes the field's divergence [4]. With a spatial map of the heliographic B_x, B_y, B_z components we derive corresponding maps of their uncertainties, computed using the noise in the observed fields, the uncertainties returned from the inversion, and then the coordinate transforms and error propagation as described in [21].

The temporal sequence of vector magnetic field maps are then aligned on a sub-pixel grid for pointing variations and trimmed for edge-data artifacts. The final data-cube consists of [x, y, B, t] and is stored in an easily accessible "structure" format of the Interactive Data Language system for analysis.

2.2 Recently Implemented Improvements and Enhancements

Over the course of this contract, the P.I. designed and implemented improvements in the following areas:

1. *Flat Field Corrections*: The flat-fielding algorithm was updated to account for the temporal variability of the observed fringe patterns; it also now determines the excess scattered light.

2. *De-Blur/De-Stretch:* This algorithm was improved both for speed and to avoid some spurious noise issues.

3. *Data-Handling:* Algorithms and procedures were developed (see appendix) to more efficiently and accurately co-align, trim, store, and analyze large numbers of magnetograms in a platform-independent manner.

2.3 Algorithm to Account for Seeing Effects:
Leka & Rangarajan, *Solar Phys.*, 2001.

The distortions in ground-based data caused by turbulence in the Earth's atmosphere are, to a large extent, minimized by the de-blur/de-stretch algorithms included in the IVM data reduction package. The overall quality of the atmospheric seeing can significantly change the inferred magnetic vector and all quantities derived from it (Figure 1). A quantitative study of the magnitude and nature of these changes was undertaken [20]. The primary results included a surprising degree of variation in derived quantities (*e.g.*, the magnitude of the vertical electric current J_z, the degree of magnetic shear, *etc.*) due to modest variation in seeing, and additionally that the variations can be region-specific (*i.e.*, the results are not generalizable between data from different active regions). A method is described for first determining, and then accounting for, the seeing-induced variations in the uncertainties for the raw data and all quantities derived from them.
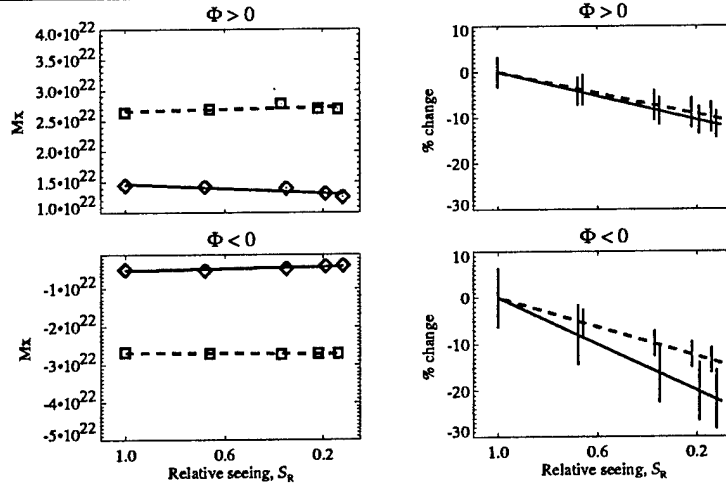
Figure 1: An example of the effects of worsening seeing on one typical parameters derived from vector magnetic field data. The total signed magnetic flux (left) for two active regions, AR7981 (——) and AR8771 (— — —), positive-polarity (top) and negative-polarity (bottom) are plotted as a function of a relative seeing measure S_R, which is simply the ratio of the blurred data to the reference data (*i.e.*, $S_R=1$ is the original dataset, $S_R < 1$ is worsening seeing. In the case of AR8771 $S_R=0.2$ resulted when a 4.4″ blur was applied to the raw images while for AR7981 the same applied blur resulted in a slightly worse S_R.) The error bars for the data points are shown, as is a linear fit to the effects of worsening seeing. For direct comparison between the two active regions, the effects are plotted as a fractional change (right). Here, the fit is plotted, and the error bars reflect the standard deviations to the fit. (From [20].)

3 Parameterization of Active Region Magnetic Distribution: Leka & Barnes *Astrophys. J.* 2003a.

3.1 Abstract

Using photospheric vector magnetic field data from the U. Hawai'i Imaging Vector Magnetograph with good spatial and temporal sampling, we study the question of identifying signatures unique to flare events in parameters derived from *B*. In this first of a series of papers we present the data analysis procedure, and present sample results focusing only on three active regions (NOAA Active Regions #8636, #8771, and #0030), two of which produced three flares (two M-class and one X-class), as compared to (most importantly) a flare-quiet epoch in a third comparable region. Quantities such as the distribution of the field, the distribution of the spatial gradients of the field, vertical current, current helicity, "twist" parameter α and magnetic shear angles, are parameterized and examined for differences in overall magnitude and evolution between the flare and flare-quiet examples. The variations expected due to atmospheric seeing changes are explicitly included. In this qualitative, "single quantity considered at a time" approach we find (1) no obvious flare-imminent signatures from the plain magnetic flux vector, the total magnetic flux, the total current current, or free energy quantities; (2) we find counter-intuitive but distinct flare-quiet implications from the mean spatial gradient of the field, the chirality-term of the vertical current, and the kurtosis of the distribution of magnetic shear angles; (3) we find flare-specific or flare-productivity signatures, although sometimes weak, using the kurtosis of the fields' spatial gradients, the mean vertical current and current-helicity densities, mean magnetic shear angles, and net current. The strongest results are, however, that (4) in ensuring a flare-unique signature, numerous potential
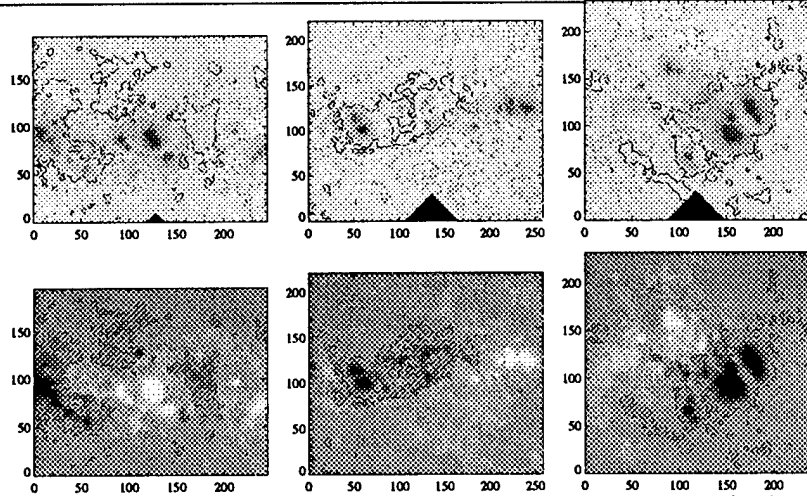
Figure 2: Images of continuum (top) and B_z (bottom, with $\pm$ 100 G contours) of NOAA AR0030 (left), AR8636 (middle) and AR8891 (right). Axes are approximately in Mm, and black triangles are masked-out field stops (adapted from [18])

---

candidate signatures (in both the variation and the overall magnitude of a parameter) are nullified on account of their behavior in a flare-quiet region, and hence (5) this qualitative "single quantity considered at a time" approach is inadequate. To address this latter point we employ a quantitative statistical approach in Paper II [19].

3.2 Example: Magnetic Flux and its distribution

The total magnetic flux is a quantitative measure of an active region's size which is well correlated with its productivity for energetic events [7, 27, 5, 31]. Using the magnetic flux as a measure of size rather than *e.g.*, the white-light area provides a more physical description of the energy available for such events. We consider here the total unsigned flux $\Phi_{tot} = \sum |B_z| \, dA$ as well as the unsigned total flux for each polarity separately $\Phi^+ = \sum (B_z > 0) \, dA$, $\Phi^- = \sum (B_z < 0) \, dA$.

We also consider the net flux imbalance $|\Phi_{net}| = |\sum B_z \, dA|$, a quantity which has been associated with flare activity [34, 31], although with little discussion as to the physical influence any (local) imbalance may have. Nonetheless we consider this quantity but take its absolute value to avoid hemispheric biases imparted by the asymmetric nature of the spatial flux distribution between preceding and following polarities.

Sample results for three active regions (of the full data considered, see Table 2),for total and net flux are shown in Figure 3. The three regions considered are comparable in size (4–6$\times 10^{22}$ Mx), although flare-quiet AR8891 is the largest. None of the regions is flux-balanced, AR8636 the farthest from balance by 10^{22} Mx; this is hardly a surprising result given a restricted (even if large) field-of-view.

Both flaring regions show small variations on the timescales shown here, with some flux growth in AR8636. However, the changes are generally not beyond the uncertainties, especially when seeing is accounted for.

The distribution of the components of the magnetic field (B_z and B_h) over the active region is quantitatively described by the statistical quantities mean, standard deviation, skew, and kurtosis. We consider the distributions of the spatially sampled (denoted by "s" rather than "(x,y)" for

4

3. Parameterization of Active Region Magnetic Distribution:

F49620-00-C-0004 Final Report
Leka & Barnes *Astrophys. J.* 2003a.

simplicity) $B_z(s)$, $B_h(s) = \sqrt{B_x(s)^2 + B_y(s)^2}$, and $B(s) = \sqrt{B_x(s)^2 + B_y(s)^2 + B_z(s)^2}$, the latter two being positive-definite quantities.

We present here the mean of the $B(s)$ distribution, the skew of the $B_z(s)$ distribution, and the skew of the $B_h(s)$ distribution (Fig. 3). The mean pixel-averaged magnetic flux similar for all three regions (400G–600G); while there is variation in this quantity prior to all flares shown here, there is similar variation during the observations of flare-quiet AR8891. The ability of skewness discriminate otherwise cloaked aspects of the fields' distribution's is clear when comparing AR0030 and AR8891: the skew of $B_z(s)$ is positive for the former but negative for the latter allowing us to identify a significant contribution from the negative tail in the latter; this is consistent with the fact that the (signed) net magnetic flux (not shown) for AR8891 is, in fact, negative. skewness shows some variation in all three regions (a marked variation in AR8636 although with similar changes due to the seeing variations). The overall skewness level of $B_h(s)$ is similar for all three regions: it is positive indicating a contribution from a high-field-strength tail, i.e., penumbral fields. The skewness increases prior to the M-flare in AR0030, shows an overall decrease before the flare in AR8636, and generally increases in AR8891.

In summary, using the distributions of the magnetic flux vector for these examples, we find no obvious and consistent difference between the flare-productive and flare-quiet regions, and no obvious and consistent evolution that occurs in the pre-flare periods.

3.3 Example: The Magnetic Helicity Density h_c

To describe the non-potential nature of the active region magnetic fields one may use the magnetic helicity [2]; a conserved quantity, the describes the linkages of magnetic systems. In practice, a number of caveats (including the possible forced state of the solar photosphere and the limitation of these data to sampling a single height in the solar atmosphere) limits what we can immediately derive to the vertical component of the current helicity density:

$$h_c(s) = B_z(s)\, \nabla_h \times B_h \tag{1}$$

$$= B_z(s) \left(\frac{\partial B_y(s)}{\partial x} - \frac{\partial B_x(s)}{\partial y} \right) \tag{2}$$

This quantity is determined spatially and as such we can examine the moments of its distribution. Additionally we compute the total (unsigned) $H_{c,tot} = \sum |h_c\, dA|$ and net (signed) $|H_{c,net}| = |\sum h_c\, dA|$ current helicity over the active regions, the latter being akin to the current helicity imbalance described in [2]. In Figure 4 the temporal variation of these quantities as well as the mean of the current helicity density distribution $\overline{h_c}$.

Interestingly, we find that overall the largest total current helicity occurs in AR8891 which is the flare-quiet region during this observing epoch. All three regions show temporal variations and one could argue there is a decrease in the total current helicity prior to the flares; there is a similar decrease during the observations in AR8891, indicating that this variation is not unique to the flaring condition. On the other hand, the *net* (signed) current helicity is significantly different from zero for both AR0030 and AR8636, while it is consistent with zero for the entire observing period for AR8891. This is consistent with some examples in [2] for their "imbalance" parameter.

Also consistent with [2] we find a larger variability in $\overline{h_c}$ for the flaring regions than with the flare-quiet AR8891, as well as a larger overall level of this quantity. Additionally, for both M-class flares one could argue a decrease in $\overline{h_c}$ occurs prior to the flare (although it is not clear such a

F49620-00-C-0004 Final Report

3. Parameterization of Active Region Magnetic Distribution:
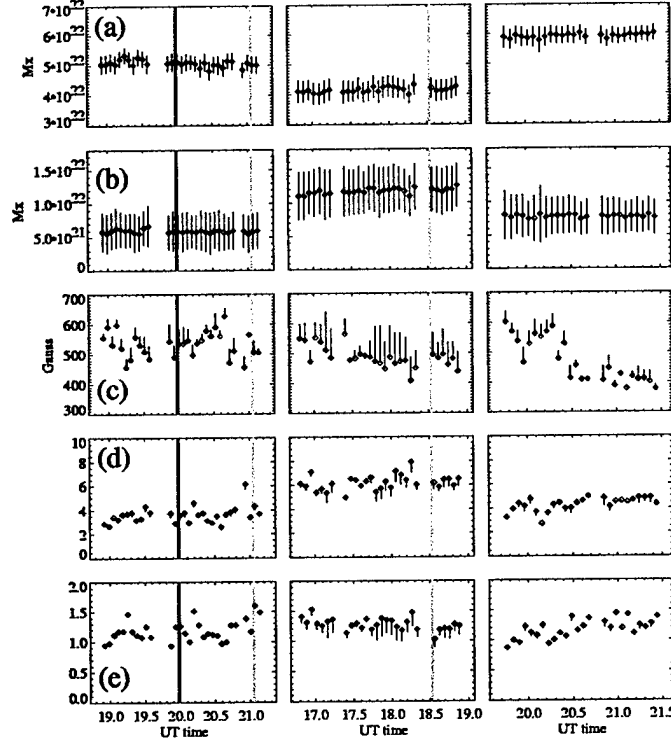Leka & Barnes *Astrophys. J.* 2003a.

Figure 3: Parameters discussed in the text for (left:right) AR0030, AR8636, and AR8891. The start-times of the flares as determined by the GOES SXR light curve are indicated by vertical grey lines, the X3.0 (thick) and M1.8 flares in AR0030, and the M1.1ERU flare in AR8636; AR8891 did not produce any flares during this epoch. The x-axes indicate the UT time, y-axes are in the relevant units, and 1-σ error bars are plotted (for the 3-σ data), including the expected variation due to measured changes in the seeing conditions (the asymmetric error bars). Shown (top:bottom) are (a) Total unsigned signed magnetic flux, (b) the absolute value of the net magnetic flux imbalance, (c) The mean (pixel-averaged) magnetic flux magnitude, (d) the kurtosis of the $B_z(s)$ distribution, and (e) the skew of the $B_h(s)$ distribution (adapted from [18]).

decrease occurs prior to the X-class flare) where no decrease of similar magnitude occurs in AR8891. A similar decrease in the magnitude of $\overline{h_c}$ is observed by [22] prior to an X-class flare in localized portions of a different active region.

To summarize, the magnetic helicity displays a number of event-unique signatures, including a small $H_{c,tot}$, significant $H_{c,net}$ and $\overline{h_c}$, and a clear decrease in $\overline{h_c}$ prior to two of the three flares.

3.4 Summary

This and our subsequent investigations begin with the null hypothesis, that there is no detectable signature of an impending energetic event. As such we have selected data to specifically *not* be biased for flaring-only regions or epochs, but to include (1) flaring epochs and (2) and flare-quiet epochs from the same region, even on the same day, and (2) flare-quiet regions which had been given a high probability of flaring (cf. Table 2). Without attempting to indict the null hypothesis it is impossible to determine whether there is a unique situation in the solar atmosphere which produces energetic events. In other words, for signature(s) to be uniquely related to solar energetic

3. Parameterization of Active Region Magnetic Distribution:

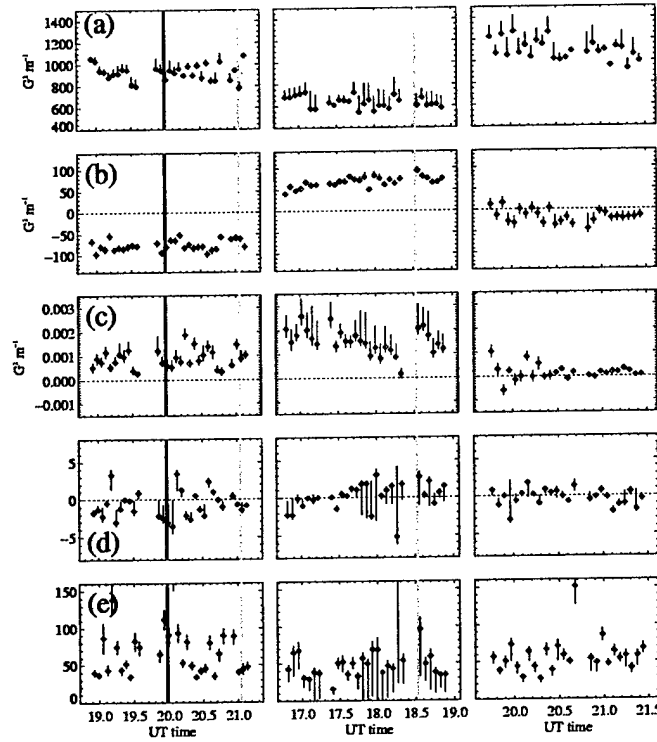F49620-00-C-0004 Final Report   Leka & Barnes *Astrophys. J.* 2003a.

Figure 4: Same as Fig. 3, but for (a) the total (unsigned) current helicity, (b) the net (signed) current helicity, (c) the mean, (d) skew, and (e) kurtosis of the current helicity density distribution.

events, they must also *not* be present at times when no energetic event is produced.

Three additional issues must be reiterated here. First, we explicitly indicate how changes in terrestrial atmospheric conditions can influence the results (*e.g.*, Figs. 3, 4). One simply cannot make *ad hoc* assumptions about the variations of the measured quantities using data which were themselves obtained under different conditions (both solar and terrestrial).

Second, *all* quantities considered here (*cf.* Table 1) are based on the physical situation at the photosphere. Observational biases have been removed (e.g., the use of heliographic-plane rather than observational-plane magnetic quantities, and the use of unsigned quantities where appropriate to avoid hemispheric biases), or acknowledged (the effect of *any* limitation on the field of view of the instrument, no matter now large, on "net" quantities, for example).

Third, by sampling the active regions both temporally and spatially, and then using the moments (and where appropriate, the total/net quantities) of the resulting spatial distributions, we parameterize the magnetic state of the photosphere and quantitatively allow for uncertainties in the data and observing conditions. In this manner, we aim to detect subtle variations caused by the evolving state of the photospheric magnetic field and avoid subjective "by-hand" examination of localized changes which might occur; the latter approach is crucial when (as we have now), the data approaches a large, statistically significant quantity.

In summary we find no obvious flare-event signatures using the parameterization of the magnetic flux vector distribution, the total current, or free energy quantities.

Counter-intuitively, we find that a broad distribution of inclination angles is unique to a flare-

4. The Discriminant Function Algorithm as applied to Flare Prediction:

F49620-00-C-0004 Final Report   Leka & Barnes *Astrophys. J.*, 2003b.

quiet episode, as is a greater mean magnitude of the spatial gradient of field-strength. The chirality-related component of the vertical current I_{net}^{ch} is larger overall for the flare-quiet region, as is the kurtosis of the shear-angle distributions.

Flare-specific signatures include weak indications of increased variability and possibly a pre-event rise in $\kappa(|\nabla_h B|)$, increased variability in I_{net}^B and slight evidence for a pre-event rise in $\overline{J_z}$ and $\kappa(J_z)$. The flare-productive regions have both a larger magnitude of the twist parameter α and a greater variation over the region, with a larger error (uncertainty) in the α_{ff} parameter for both flare-productive regions. The magnetic helicity density and its parameterizations show a number of unique flare-event signatures, including significant $H_{c,net}$ and $\overline{h_c}$ for the immediately flare-productive regions, and a clear decrease in the latter prior to two of the three events detailed in [18]. We do find that magnetic shear was larger and more widespread in the flare-producing regions.

When pre-event variations and levels are examined using both flare-producing and flare-quiet regions, the obvious, and event-unique signatures are rare. We do focus on only three regions and as many flare events here; in [19] (see §4, below) we take an in-depth, statistical look at the question of flare-unique signatures.

4 The Discriminant Function Algorithm as applied to Flare Prediction: Leka & Barnes *Astrophys. J.*, 2003b.

4.1 Abstract

Using Imaging Vector Magnetograph observations of photospheric vector magnetic fields in seven active regions, we apply discriminant analysis to the wide range of parameters discussed in Paper I (Leka & Barnes 2003, cf. §3, above). We treat the mean value and the rate of change of each parameter as a separate variable. In order to discover which of these properties are associated with flaring, we begin by considering pairs of variables. Applying Hotelling's T^2-test to the data, we find that a number of properties show statistical differences between flaring and flare-quiet regions. However, discriminant functions of pairs of variables have high error rates, implying a large degree of overlap in the properties of flaring and flare-quiet regions. To reduce this overlap, we simultaneously consider larger numbers of variables. This results in much lower estimates for the error rate, but we can find no unique combination of variables which is significantly better than other combinations. Our sample sizes are too small for us to directly compare the predictive power of large numbers of variables, to determine which are the most important in flaring. Instead, we consider discriminant functions of all possible permutations of four variables. We rank the permutations based on the probability that the samples come from different populations, and look for the most frequently appearing variables in the best permutations. We present these variables as the most likely to be associated with flaring. Individually, these variables may have little ability to distinguish between flaring and flare-quiet regions, so it is important to consider combinations of several variables. We construct a single discriminant function of ten variables to support our method of selecting the most frequently occurring variables as being the most important in flaring.

F49620-00-C-0004 Final Report

Table 1: Parameters used in the discriminant analysis

variable	description
$s = \mathrm{median}(\Delta I)$	seeing, *i.e.*, median of the granulation contrast
Distribution of Magnetic Fields	
vertical magnetic field	$B_z = \mathbf{B} \cdot \mathbf{e}_z$
$\overline{B_z}$	mean of vertical magnetic field
$\sigma(B_z)$	standard deviation of vertical magnetic field
$\varsigma(B_z)$	skew of vertical magnetic field
$\kappa(B_z)$	kurtosis of vertical magnetic field
$\Phi_{tot} = \sum |B_z|\, dA$	total unsigned flux
$|\Phi_{net}| = |\sum B_z\, dA|$	absolute value of the net flux
horizontal magnetic field	$B_h = \sqrt{B_x^2 + B_y^2}$
$\overline{B_h}$	mean of horizontal magnetic field
$\sigma(B_h)$	standard deviation of horizontal magnetic field
$\varsigma(B_h)$	skew of horizontal magnetic field
$\kappa(B_h)$	kurtosis of horizontal magnetic field
Distribution of Magnetic Field Spatial Gradients	
gradient of total field	$|\nabla_h B| = \sqrt{(\partial B/\partial x)^2 + (\partial B/\partial y)^2}$
$\overline{|\nabla_h B|}$	mean of gradient of field
$\sigma(|\nabla_h B|)$	standard deviation of gradient of field
$\varsigma(|\nabla_h B|)$	skew of gradient of field
$\kappa(|\nabla_h B|)$	kurtosis of gradient of field
gradient of vertical field	$|\nabla_h B_z| = \sqrt{(\partial B_z/\partial x)^2 + (\partial B_z/\partial y)^2}$
$\overline{|\nabla_h B_z|}$	mean of gradient of vertical field
$\sigma(|\nabla_h B_z|)$	standard deviation of gradient of vertical field
$\varsigma(|\nabla_h B_z|)$	skew of gradient of vertical field
$\kappa(|\nabla_h B_z|)$	kurtosis of gradient of vertical field
gradient of horizontal field	$|\nabla_h B_h| = \sqrt{(\partial B_h/\partial x)^2 + (\partial B_h/\partial y)^2}$
$\overline{|\nabla_h B_h|}$	mean of gradient of horizontal field
$\sigma(|\nabla_h B_h|)$	standard deviation of gradient of horizontal field
$\varsigma(|\nabla_h B_h|)$	skew of gradient of horizontal field
$\kappa(|\nabla_h B_h|)$	kurtosis of gradient of horizontal field
Vertical Current Density	
vertical current density	$J_z = (\partial B_y/\partial x - \partial B_x/\partial y)/\mu_0$
$\overline{J_z}$	mean of vertical current density
$\sigma(J_z)$	standard deviation of vertical current density
$\varsigma(J_z)$	skew of vertical current density
$\kappa(J_z)$	kurtosis of vertical current density
$I_{tot} = \sum |J_z|\, dA$	total unsigned current
$I_{net} = |\sum J_z\, dA|$	absolute value of the net current
$I_{net}^B = |\sum J_z(B_z > 0)\, dA| + |\sum J_z(B_z < 0)\, dA|$	sum of absolute value of net currents in each polarity
vertical component of hetergeneity current density[33]	$J_z^h = (b_y \partial B_x/\partial y - b_x \partial B_y/\partial x)/\mu_0$
$\overline{J_z^h}$	mean of vertical hetergeneity current density
$\sigma(J_z^h)$	standard deviation of vertical hetergeneity current density
$\varsigma(J_z^h)$	skew of vertical hetergeneity current density
$\kappa(J_z^h)$	kurtosis of vertical hetergeneity current density
$I_{tot}^h = \sum |J_z^h|\, dA$	total unsigned hetergeneity current
$I_{net}^h = |\sum J_z^h\, dA|$	absolute value of the net hetergeneity current

F49620-00-C-0004 Final Report

4. The Discriminant Function Algorithm as applied to Flare Prediction:
Leka & Barnes *Astrophys. J.*, 2003b.

Table 1: – Continued

variable	description
Current Helicity	
current helicity[2]	$h_c = CB_z(\partial B_y/\partial x - \partial B_x/\partial y)$
$\overline{h_c}$	mean of current helicity
$\sigma(h_c)$	standard deviation of current helicity
$\varsigma(h_c)$	skew of current helicity
$\kappa(h_c)$	kurtosis of current helicity
$H_{c,tot} = \sum |h_c\,dA|$	total unsigned current helicity
$|H_{c,net}| = |\sum h_c\,dA|$	absolute value of net current helicity
Inclination Angle	
inclination andle	$\gamma = \tan^{-1}(B_z/B_h)$
$\overline{\gamma}$	mean of inclination angle
$\sigma(\gamma)$	standard deviation of inclination angle
$\varsigma(\gamma)$	skew of inclination angle
$\kappa(\gamma)$	kurtosis of inclination angle
Shear Angle	
3-D Shear Angle[32]	$\Psi = \cos^{-1}(B^p \cdot B^o / B^p B^o)$
$\overline{\Psi}$	mean of shear angle
$\sigma(\Psi)$	standard deviation of shear angle
$\varsigma(\Psi)$	skew of shear angle
$\kappa(\Psi)$	kurtosis of shear angle
$A(\Psi > 45°)$	area with shear > 45°
$A(\Psi > 80°)$	area with shear > 80°
$\overline{\Psi_{NL}}$	mean of neutral line shear angle
$\sigma(\Psi_{NL})$	standard deviation of neutral line shear angle
$\varsigma(\Psi_{NL})$	skew of neutral line shear angle
$\kappa(\Psi_{NL})$	kurtosis of neutral line shear angle
$L(\Psi_{NL} > 45°)$	length of neutral line with shear > 45°
$L(\Psi_{NL} > 80°)$	length of neutral line with shear > 80°
Horizontal Shear Angle	$\psi = \cos^{-1}(B_h^p \cdot B_h^o / B_h^p B_h^o)$
$\overline{\psi}$	mean of horizontal shear angle
$\sigma(\psi)$	standard deviation of horizontal shear angle
$\varsigma(\psi)$	skew of horizontal shear angle
$\kappa(\psi)$	kurtosis of horizontal shear angle
$A(\psi > 45°)$	area with horizontal shear > 45°
$A(\psi > 80°)$	area with horizontal shear > 80°
$\overline{\psi_{NL}}$	mean of neutral line horizontal shear angle
$\sigma(\psi_{NL})$	standard deviation of neutral line horizontal shear angle
$\varsigma(\psi_{NL})$	skew of neutral line horizontal shear angle
$\kappa(\psi_{NL})$	kurtosis of neutral line horizontal shear angle
$L(\psi_{NL} > 45°)$	length of neutral line with horizontal shear > 45°
$L(\psi_{NL} > 80°)$	length of neutral line with horizontal shear > 80°

4. The Discriminant Function Algorithm as applied to Flare Prediction:

F49620-00-C-0004 Final Report   Leka & Barnes *Astrophys. J.*, 2003b.

Table 1: – Continued

variable	description
	Twist Parameter
twist parameter	$\alpha = C J_z / B_z$
$\overline{\alpha}$	mean of twist
$\sigma(\alpha)$	standard deviation of twist
$\varsigma(\alpha)$	skew of twist
$\kappa(\alpha)$	kurtosis of twist
best fit α_{ff}[21]	$B = \alpha_{ff} \nabla \times B$
$|\alpha_{ff}|$	absolute value of best fit α_{ff}
	Pseudo-Free Energy
pseudo-free energy density[32]	$\rho_f = (B^p - B^o)^2 / 8\pi$
$\overline{\rho_f}$	mean of free energy
$\sigma(\rho_f)$	standard deviation of free energy
$\varsigma(\rho_f)$	skew of free energy
$\kappa(\rho_f)$	kurtosis of free energy
$E_f = \sum \rho_f \, dA$	total free energy

For each of these parameters, we consider the mean value for an epoch, denoted by $\langle\rangle$ and the slope of a regression line, denoted by d/dt.

4.2 Discriminant Analysis

Our problem is essentially one of statistical discrimination: measurements of a number of parameters derived from the photospheric vector field data (*cf.* §3) come from samples of two populations: flare events or flare-quiet events. The goal is to determine whether the two populations are statistically different from each other, based on those measurements. If they are statistically different from each other, then given a new data point the question is how to classify it as belonging to one group of the other. The differences are evaluated by performing Hotelling's T^2-test, and we construct discriminant functions in order to predict group membership [11, 1]. The discriminant function is constructed to maximize correct predictions while at the same time maintaining equal probabilities for predicting that a region will flare when it does not, and for predicting that a region will not flare when it does.

The most straightforward way to test how well the function discriminates between flaring and non-flaring regions is to construct a classification or "truth" table. Unfortunately, it can be shown that this method always underestimates the number of incorrect predictions [10]. Other methods can place stricter bounds on the probability of misclassification. For example, constructing a discriminant function with one data point left out, and using that discriminant function to classify the excluded point, then repeating this for all data points gives an unbiased estimate of the error rate for the discriminant function with $n - 1$ data points. In the limit of large n, this will be an estimate of the actual error rate for the n data point case. Our sample sizes are sufficiently small that we restrict our use of this approach to illustration only.

The limitations of these procedures include the following. A high probability that the samples come from different populations does not necessarily mean that the discriminant function will have a low error rate in predicting membership for future observations. For example, two samples may have significantly different but also a significant scatter such that there results a great deal of overlap in parameter space. A discriminant function will never have a low error rate for such a situation. However, if the actual error rate can be accurately estimated, then the combination of the significance of the difference in the samples combined with the estimate of the error rate can be used to learn something about the samples. If the samples are significantly different and the actual error rate is low, then the samples occupy distinct regions in the space of the variables used in the discriminant function. This is the ideal case, in which it is possible to definitively describe those physical properties of an active region sufficient and necessary for it to flare. If the error rate is high, despite a significant difference between the samples, then there is a great deal of overlap

Table 2: Active Regions used in Discriminant Analysis

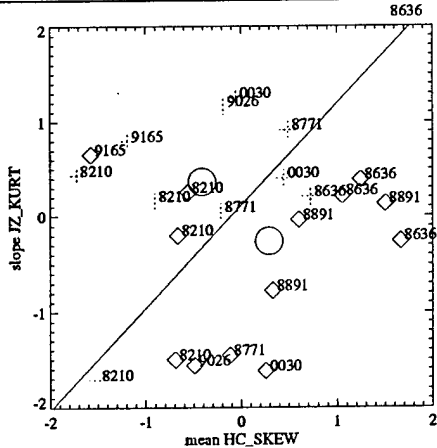| NOAA AR number	Date	Coordinates	Area (μH)	Mag. class	McIntosh class	Observed GOES SXR flares
8210	1998 May 01	S18 W05	270	$\beta\gamma$	Cho	C2.8, C2.6, M1.2
8636	1999 Jul 23	N20 E04	550	$\beta\gamma\delta$	Fki	M1.1
8771	1999 Nov 25	S15 W48	750	$\beta\gamma$	Eki	C1.6, M2.0
8891	2000 Mar 01	S15 E11	1030	$\beta\gamma$	Eki	...
9026	2000 Jun 05	N22 E20	870	$\beta\gamma\delta$	Fki	C3.8
9165	2000 Sep 15	N13 E03	140	$\beta\gamma$	Dai	C7.4
0030	2002 Jul 15	N18 E03	781	$\beta\gamma\delta$	Fkc	X3.0, M1.8

Figure 5: The discriminant function for the variables $[\langle\varsigma(h_c)\rangle,\ d\kappa(J_z)/dt]$. Flaring epochs (+) are color coded for the Soft X-Ray flare class, C (green) M (orange) and X (red); quiet epochs are also indicated (◇). Each epoch is labeled with its parent NOAA AR number. The means of each sample are shown with circles, and the resulting discriminant function is the solid line.

in the parameter space. This suggests that there is an additional physical property necessary to produce an energetic event. In order to make either of the above statements, an accurate estimate of the actual error rate must be available which is not generally the case. The number of incorrect predictions in the classification table provides a lower bound, and better estimates can be made, particularly for large sample sizes, but the actual error rate will not be known.

4.3 Application to IVM Data

For this study, Imaging Vector Magnetograph data for all seven active regions (see Table 2) are included. Each time sequence of magnetograms is divided into different epochs, based on the occurrences of flares and on time gaps in the data. For this demonstration, we have a group of 10 flaring epochs, and a group of 14 non-flaring epochs.

The behavior of each parameter in an epoch is described by its weighted mean, *i.e.*, the parameter's overall magnitude, and the slope of a weighted regression line fit to the temporally sampled data, *i.e.*, the temporal rate of change of the parameter in question. A complete list of the parameters considered is given in Table 1.

4.3.1 A Two Variable Discriminant Function

We first consider the combination of the mean of the skew of the current helicity, $\langle\varsigma(h_c)\rangle$ and the slope of the kurtosis of the vertical current, $d\kappa(J_z)/dt$. Using these two variables alone, the probability that the samples are from distinct populations is 0.95, the highest probability of any variable pair. The discriminant function for this case is

$$f(\langle\varsigma(h_c)\rangle, \frac{d\kappa(J_z)}{dt}) \ = \ 0.12 - 1.10\langle\varsigma(h_c)\rangle + 1.03\frac{d\kappa(J_z)}{dt} \tag{3}$$

in standardized variables. The nearly equal magnitudes of the resulting coefficients implies that they have approximately equal predictive power. This function, along with the data from which it

13

4. The Discriminant Function Algorithm as applied to Flare Prediction:

F49620-00-C-0004 Final Report   Leka & Barnes *Astrophys. J.*, 2003b.

was constructed, is shown in Figure 5. Note that in this case, there is neither obvious clustering of different epochs from the same active region, nor of the flare classes.

Table 3: 2-Variable Discriminant Function Classification Table

		predicted	
		flare	no flare
observed	flare	7	3
	no flare	4	10

The classification table for this discriminant function is shown in Table 3; from either the table, or by directly inspecting the figure, one finds that seven of twenty-four classifications were made incorrectly, for an error rate of 0.29. The "$n - 1$ data points" method (outlined above) results in an estimated error rate identical to the table. Hence, despite the high probability for distinct populations, the high estimates for the error rate suggest that these two variables alone are insufficient to clearly distinguish flaring from flare-quiet epochs.

4.3.2 Six Variable Discriminant Functions

To improve upon the error rate for predicting the membership of a new observation, the analysis must be performed by considering more variables simultaneously. Ideally, a single discriminant function is constructed of all the variables, and the relative magnitudes of the coefficients are used to estimate the predictive power of each parameter relative to the others. However, due to our small sample sizes we are currently unable to consider more than a few variables simultaneously. Still, by considering all the possible permutations of parameters for a given number of variables, we can sort the statistical results to determine the best discriminant function of that number of variables.

Doing this for the four-variable case, we take the variables appearing most frequently in the best discriminant functions to be the parameters with the most predictive power (this approach for greater than four variables becomes prohibitive since the number of permutations grows so rapidly). Nevertheless, using the best four-variable cases as starting points, we are able to arrive at several interesting examples of discriminant functions of *six* variables. One such example is

$$f = 1.2 + 31.0 \langle \overline{|\nabla_h B_z|} \rangle + 6.9 \langle \varsigma (|\nabla_h B_h|) \rangle + 10.4 \langle I^B_{net} \rangle + 81.5 \langle \overline{\Psi} \rangle + 66.6 \langle \varsigma(\psi) \rangle + 7.2 \frac{d|H_{c,net}|}{dt} \quad (4)$$

in standardized variables (see Table 1 for variable descriptions). The probability that flaring and flare-quiet epochs come from different populations for these variables is 0.999999, and the discriminant function is able to successfully classify *all* of the data points, *i.e.*, the error rate is 0.0 (see Table 4). However, this is an example of using a truth table with caution: the "$n - 1$ data points" error-estimation method gives an error rate estimated at 0.083.

A second interesting example the discriminant function

$$f = 1.0 - 38.8 \langle \Phi_{tot} \rangle + 6.8 \langle \varsigma(|\nabla_h B_h|) \rangle + 36.8 \langle I_{tot} \rangle + 27.6 \langle \sigma(\Psi) \rangle + 33.6 \langle \kappa(\psi) \rangle + 2.1 \frac{d|H_{c,net}|}{dt} \quad (5)$$

in standardized variables, which results in a different-population probability of 0.999996, and the discriminant function mis-classifies one data point for an error rate of 0.042 (see Table 4), identical to the estimated actual error rate derived from the "$n - 1$" approach.

14

F49620-00-C-0004 Final Report

5. Quantifying the Coronal Topology with the Magnetic Charge Topology
Barnes, Leka & Longcope *Astrophys. J.*, 2003.

Table 4: 6-Variable Discriminant Function Classification Tables

		predicted					predicted	
		flare	no flare				flare	no flare
observed	flare	10	0	observed		flare	9	1
	no flare	0	14			no flare	0	14

Evidently, there exist combinations of variables for which flaring and flare-quiet epochs occupy quite different regions in phase space. The fact that there are only two variables which appear in *both* examples above suggests that discriminant functions of larger numbers of variables would be preferable, since there are distinctions between the groups which are not being made in each example. However, to do this simply requires more data.

4.4 Summary

While flaring and flare-quiet epochs appear to be statistically different for groups of variables or even some *pairs* of variables, at this time we find no single, or even small number of, physical properties of an active region which directly results in flaring. We do demonstrate, however, that to accurately predict which active regions will flare, many variables must be considered simultaneously. By considering all permutations of four variable discriminant functions, we conclude that the active regions which flare are likely to have: an increasing kurtosis of the vertical current, $d\kappa(J_z)/dt$, an increasing kurtosis of the twist parameter, $d\kappa(\alpha)/dt$, a decreasing kurtosis of the current helicity, $d\kappa(h_c)/dt$, and a large mean and standard deviation of the neutral line horizontal shear angle, $\langle\overline{\psi_{NL}}\rangle$ and $\langle\sigma(\psi_{NL})\rangle$. The kurtosis of a distribution describes the non-normal appearance of either of a distribution's wings; thus these properties roughly correspond to having an increase in the magnitudes of the strongest vertical currents, an increase in the strongest twist parameters, a decrease in the strongest magnitudes of the current helicity and a neutral line along which the field is highly non-potential. Other properties are likely to be necessary for flaring, but these are the most frequently occurring properties in our best four variable discriminant functions.

Our six variable examples indicate that while combinations can be found which result in quite good predictions, the combinations are not unique and hence larger numbers of variables need to be considered simultaneously. To do this requires more data in order to simply consider more variables and also to make accurate estimates of the error rates.

5 Quantifying the Coronal Topology with the Magnetic Charge Topology
Barnes, Leka & Longcope *Astrophys. J.*, 2003.

One of the great difficulties encountered in trying to understand solar flares is that one must generally understand the magnetic field in the corona, where the flare-onset energy release occurs, using extrapolations from measurements of vector magnetic fields at the photosphere. The Minimum Current Corona (MCC) model [24] is one approach which has shown some success. This model has been applied to a single magnetogram of NOAA AR 6993/6994 [26], and was able to predict some of the field lines along which the flares appeared to occur. The MCC is an extension of the Magnetic Charge Topology (MCT) models discussed by numerous authors [3, 8, 30, 16, 6, 29].

In the MCT models, the photospheric B_z field is used to derive the locations and strengths

5. Quantifying the Coronal Topology with the Magnetic Charge Topology

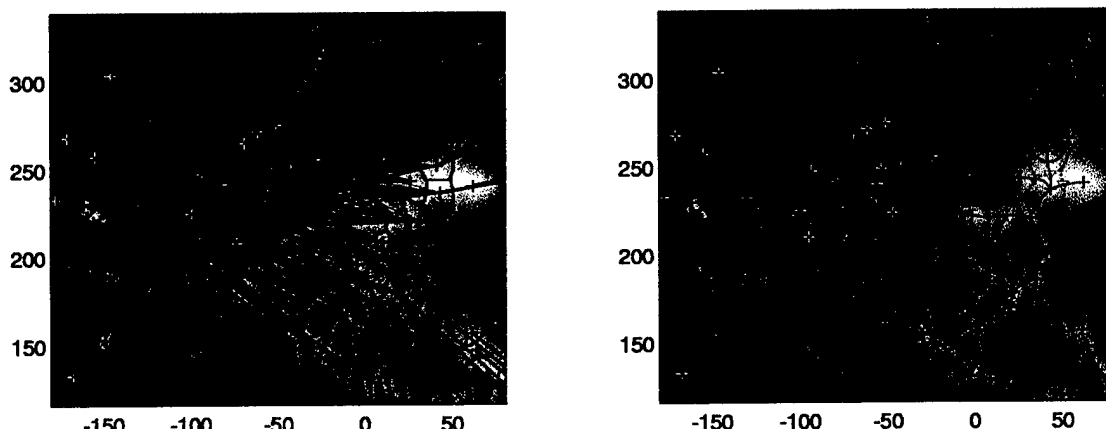F49620-00-C-0004 Final Report   Barnes, Leka & Longcope *Astrophys. J.*, 2003.

Figure 6: One magnetogram from NOAA AR 8636, showing the smoothed field, the pole locations, the boundaries of the partitions defining the pole locations (black lines) and the connections between poles (blue lines) in the left panel, and the locations of the poles and nulls (blue, red and orange), the null spines (solid black lines), the fan traces (dotted black lines) and some of the separators (green lines) in the right panel.

of a set of magnetic monopoles; the field everywhere above the photosphere is then assumed to be due only to these monopoles. Knowing the magnetic field, we can in principle determine the locations of magnetic null points, where the magnetic field vector vanishes. In this approximation, each field line begins and ends on a monopole or null (or at infinity), which provides a way to quantify the topology of the coronal magnetic field. We define the connectivity matrix, ψ_{ij}, as the flux connecting the ith pole to the jth pole. The surfaces which bound the flux bundles joining two poles are known as separatrix surfaces. The intersection of two separatrix surfaces is a separator, which is a field line connecting two null points. It has been shown [9, 17] that separators are the site of magnetic reconnection, and hence likely to be the site of energy release in flaring.

5.1 Application of MCT to IVM data

We have adapted the code developed by Dr. D.W. Longcope to apply the MCT model to time-series of IVM data for several active regions (*cf.* Table 2). The code had previously been applied to a single lower spatial-resolution magnetogram of a simple active region; as such, it has required extensive modification to be used with our datasets. First, the magnetogram is smoothed, using a potential field extrapolation; only areas of the magnetograms in which the measured vertical field strength is not consistent with zero are used, determined by the measured noise levels. The remaining part of the magnetogram is partitioned using a downhill gradient method where every pixel is associated with its local maximum or minimum. This results in such a large number of partitions as to be unwieldy, so partitions with small flux are merged with their closest neighbor of the same polarity, provided that neighbor is within a maximum distance. Our motivation in doing this is to simplify areas of plage, where small variations in field strength over large areas can result in many small partitions, while retaining strong partitions with polarity opposite to their surroundings, such as delta spots. Each final partition is then represented by a magnetic pole, the strength of which is determined by the total flux of the partition, and the location of which is the flux-weighted average position of the partition (Figure 6).

The connectivity matrix is calculated using a Monte-Carlo method to select field lines emanating
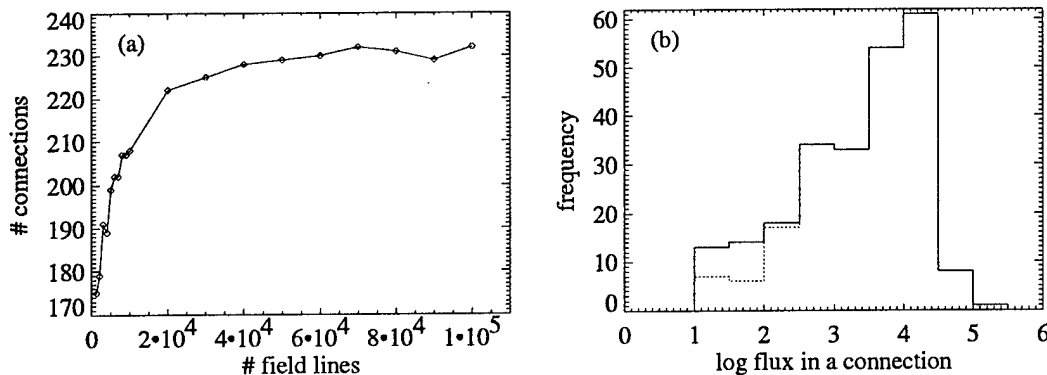
Figure 7: Panel (a) shows the number of connections found as a function of the number of field lines used in the calculation. Panel (b) plots the number of connections found as a function of the log of the flux in the connections for the case of 2×10^5 field lines (solid line) and the case of 2×10^4 field lines (dotted line).

from one pole and tracing them to their termination on another pole (or at infinity). In the initial application of the code, 300 field lines originating on the positive poles, and an equal number originating on the negative poles, were sufficient to calculate the connectivity. In applying it to IVM data, we found 300 to be severely inadequate (Figure 7). We have modified Dr. Longcope's initial approach to use at least 2×10^4 field lines, with the fraction of these field lines originating from a given pole determined by the fraction of the total flux it contains, with a minimum of 10 field lines. In Figure 7(a) we show the number of connections found as a function of the number of field lines used in the calculation for one magnetogram; N.B., the result for 300 is not even shown. While we risk missing some connections even with 2×10^4 field lines, using a significantly higher number is prohibitively time consuming. Additionally, we have determined that the connections which are missed are preferentially those with very small fluxes [see Figure 7(b)], which are unlikely to contribute significantly to flaring activity.

In addition to the connectivity matrix, we calculate the locations of null points and separators. The original null-finding procedure from Dr. Longcope was unable to find all of the nulls in complicated pole arrangements such as those we presented. We have improved upon the algorithm, but in essence the problem is one of multi-dimensional root finding, for which there exists no general solution. Likewise, tracing the separators depends on following a single field line from which neighboring field lines are exponentially diverging. In some cases, this can be accomplished, but not in general. Figure 6 shows, as a figure, the connectivity matrix ψ_{ij}, the locations of the nulls and of some separators. Note that all these quantities are not independent. When only prone photospheric nulls are present [25],

$$N_{sep} = N_c - N_n - 1 \tag{6}$$

where N_{sep} is the number of separators above the photosphere, N_c is the number of connections and N_n is the number of nulls. Our MCT models of IVM data contain other types of nulls (upright nulls), which can also result in separators lying in the plane of the photosphere. In conjunction with Dr. Longcope, we hope to expand this treatment to allow for such nulls and separators to more adequately represent the observations.
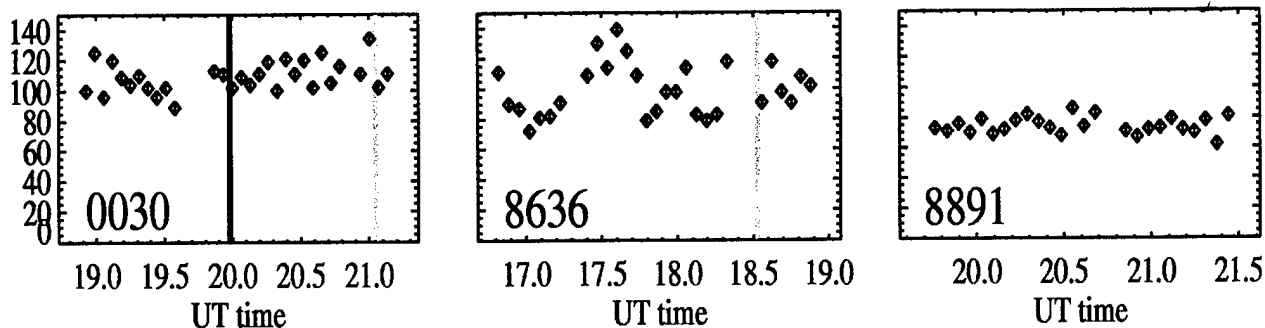
17

Figure 8: The time evolution of the number of separators for NOAA AR 0030, 8636 and 8891. The red line indicates the time of an X-class flare, while the yellow lines indicate the times of M-class flares.

5.2 Quantifying the Coronal Topology: Sample Results

In essence, this is the foundation for the MCT model; evolving this model in time leads to currents along separators, which is the origin of the term Minimum Current Corona. However, even before considering the currents, we can quantify the complexity of the coronal magnetic field using the information contained in the connectivity matrix and related quantities. For example, since reconnection is likely to occur at the intersection of separatrix surfaces, we consider the evolution of the number of separators (Figure 8), as determined by equation (6). Three active regions are studied in detail, two of which flared during the period of observation (NOAA AR 8636, 0030), while the third did not (NOAA AR 8891). Although there is significant scatter in the number of separators, the regions which flared do generally have significantly more separators than the region which did not flare.

The MCT model can be used to quantitatively characterize the properties of the coronal magnetic field, rather than the directly measured photospheric field. In the context of flare prediction, we can consider three broad categories of possible flare-predicting parameters, with some overlap. The first category simply measures the overall complexity of a region. If the reconnection which powers a flare is a means of simplifying the topology of the coronal field, then presumably the field must start with a certain amount of complexity, and more complex regions are more likely to flare. The second category looks for a trigger for a flare. For example, the emergence of new flux into an existing active regions is thought to be a mechanism for triggering a flare. Finally, if flares are indeed associated with reconnection along a separator, then such separators must be present in an active region, and we can consider the number of possible locations at which a flare can occur. Whether parameters describing any of these categories will prove useful in flare prediction must be tested on a statistical basis. With the discriminant analysis already applied to the photospheric parameters (cf. §4), we have the machinery in place to make such a test of inferred coronal parameters.

6 Summary of Accomplishments

To summarize, in the last three years of effort under this contract, we have:
- Acquired, reduced and prepared IVM data for six active regions for analysis; this includes selecting target regions that included flare-productive and, as counter-examples, flare-quiet epochs.

18

• Developed a successful method for access, storage, and manipulation of large magnetogram data-sets using a platform-independent approach.

• Developed an algorithm to model, and account for, the seeing-induced variations in the observed vector magnetic field data and quantities derived from it.

• Derived and examined the magnitude and variation of more than 80 parameters that describe the magnetic state of the solar photosphere as it relates to flare events.

• Developed a statistical approach based on Discriminant Function Analysis and Hotelling's T^2-test, to evaluate the possibility of distinguishing between flare-imminent and flare-quiet active regions and epochs using the parameterizations derived from time-sequences of vector magnetic field data.

• Applied the statistical tests to the 24 flare-productive and flare-quiet epochs available, deriving preliminary lists of parameters which may be useful to both the flare-prediction and the modeling communities.

• Attempted to apply the Magnetic Charge Topology method to quantifying the coronal topology and its complexity. Upon discovery that the codes as delivered to us from Dr. Longcope were not suited for data as complex as the flaring active regions require, we have embarked upon substantial modifications to the codes (which are being developed in collaboration with Dr. Longcope and shared with him).

• Nonetheless, we have presented a preliminary example of the temporal evolution of the coronal complexity in three active regions.

7 References

References

[1] Anderson, T. W.: 1984, *An Introduction to Multivariate Statistical Analysis*. New York: Wiley.

[2] Bao, S., H. Zhang, G. Ai, and M. Zhang: 1999, 'A Survey of Flares and Current Helicity in bctive Regions'. *Astron. Astrophys. Supp. Ser.* **139**, 311–320.

[3] Baum, P. and A. Bratenahl: 1980, 'Reference to be inserted here'. *Solar Phys.* **67**, 240.

[4] Canfield, R. C., J. F. de La Beaujardière, Y. Fan, K. D. Leka, A. N. McClymont, T. Metcalf, D. L. Mickey, , J.-P. Wülser, and B. W. Lites: 1993, 'The Morphology of Flare Phenomena, Magnetic Fields, and Electric Currents in Active Regions I. Introduction and Methods'. *Astrophys. J.* **411**, 362–369.

[5] Canfield, R. C., H. S. Hudson, and D. E. McKenzie: 1999, 'Sigmoidal Morphology and Eruptive Solar Activity'. *Geophys. Res. Lett.* **26, No. 6**, 627–630.

[6] Démoulin, P., J. Hénoux, and C. Mandrini: 1994, 'Reference to be inserted here'. *Astron. Astrophys.* **285**, 1023.

[7] Giovanelli, R. G.: 1939, 'The Relations between Eruptions and Sunspots'. *Astrophys. J.* **89**, 555–567.

[8] Gorbachev, V. S. and B. Somov: 1988, 'Reference to be inserted here'. *Solar Phys.* **117**, 77.

[9] Greene, J. M.: 1988, 'Geometrical properties of three-dimensional reconnecting magnetic fields with nulls'. *J. Geophys. Res.* **93**, 8583–8590.

[10] Hills, M.: 1966, 'Allocation Rules and their Error Rates'. *J. R. Statist. Soc. B* **28**, 1–31.

[11] Kendall, M., A. Stuart, and J. K. Ord: 1983, *The Advanced Theory of Statistics*, Vol. 3. New York: Macmillan Publishing Co., Inc, 4th edition.

[12] Labonte, B. and K. D. Leka: 2002, 'The Imaging Vector Magnetograph at Haleakala III: Determining The Magnetic Atmosphere'. *Solar Phys.* p. (in preparation).

[13] Labonte, B., D. L. Mickey, and K. D. Leka: 1999, 'The Imaging Vector Magnetograph at Haleakala II: Reconstruction of Stokes Spectra'. *Solar Phys.* **189**, 1–24.

[14] Landolfi, M. and E. Landi Degl'Innocenti: 1982, 'Magneto-Optical Effects and the Determination of Vector Magnetic Fields from Stokes Profiles'. *Solar Phys.* **78**, 355–364.

[15] Landolfi, M., E. Landi Degl'Innocenti, and P. Arena: 1984, 'On the Diagnostic of Magnetic Fields in Sunspots Through the Interpretation of Stokes Parameter Profiles'. *Solar Phys.* **93**, 269–287.

[16] Lau, Y.-T.: 1993, 'Reference to be inserted here'. *Solar Phys.* **148**, 301.

[17] Lau, Y.-T. and J. M. Finn: 1990, 'Reference to be inserted here'. *Astrophys. J.* **350**, 672.

[18] Leka, K. D. and G. Barnes: 2003a, 'Photospheric Magnetic Field Properties of Flaring *vs.* Flare-Quiet Active Regions I: Data, General Analysis Approach, and Sample Results'. *Astrophys. J.* p. submitted.

[19] Leka, K. D. and G. Barnes: 2003b, 'Photospheric Magnetic Field Properties of Flaring *vs.* Flare-Quiet Active Regions II: Applying a Discriminant Function'. *Astrophys. J.* p. submitted.

[20] Leka, K. D. and K. E. Rangarajan: 2001, 'Effects of 'Seeing' on Vector Magnetograph Measurements'. *Solar Phys.* **203**, 239–254.

[21] Leka, K. D. and A. Skumanich: 1999, 'On the value of "α" from Vector Magnetograph Measurements, I: Measurement, Errors, and Caveats'. *Solar Phys.* **188**, 3–19.

[22] Liu, Y. and H. Zhang: 2002, 'Analysis of a Delta Spot'. *Astron. Astrophys.* **386**, 646–652.

[23] Longcope, D.: 1996a, 'Topology and Current Ribbons: A Model for Current, Reconnection and Flaring in a Complex, Evolving Corona'. *Solar Phys.* **169**, 91–121.

[24] Longcope, D. W.: 1996b, 'Topology and Current Ribbons: A Model for Current, Reconnection and Flaring in a Complex, Evolving Corona'. *Solar Phys.* **169**, 91–121.

[25] Longcope, D. W. and I. Klapper: 2002, 'A General Theory of Connectivity and Current Sheets in Coronal Magnetic Fields Anchored to Discrete Sources'. *Astrophys. J.* **579**, 468–481.

[26] Longcope, D. W. and A. V. R. Silva: 1998, 'A Current Ribbon Model for Energy Storage and Release with Application to the Flare of 7 January 1992'. *Solar Phys.* **179**, 349–377.

[27] McIntosh, P. S.: 1990, 'The Classification of Sunspot Groups'. *Solar Phys.* **125**, 251–267.

[28] Mickey, D. L., R. Canfield, B. J. LaBonte, K. D. Leka, M. F. Waterson, and H. M. Weber: 1996, 'The Imaging Vector Magnetograph at Haleakalā'. *Solar Phys.* **168**, 229–250.

[29] Parnell, C. E., E. R. Priest, and L. Golub: 1994, 'Reference to be inserted here'. *Solar Phys.* **151**, 57.

[30] Priest, E. R. and T. G. Forbes: 1989, 'Reference to be inserted here'. *Solar Phys.* **119**, 211.

[31] Tian, L., Y. Liu, and J. Wang: 2002, 'The Most Violent Super-Active Regions in the 22nd and 23rd Cycles'. *Solar Phys.* **209**, 361–374.

[32] Wang, J., Z. Shi, H. Wang, and Y. Lü: 1996, 'Flares and the Magnetic Nonpotentiality'. *Astrophys. J.* **456**, 861–878.

[33] Zhang, H.: 2001, 'Electric Current and Magnetic Shear in Solar Active Regions'. *Astrophys. J. Letters* **557**, 71–74.

[34] Zhang, H., G. Zi, X. Yan, W. Li, and Y. Liu: 1994, 'Evolution of Vector MAgnetic Field and White-Light Flares in a Solar Active Region (NOAA 6659) in 1991 June'. *Astrophys. J.* **423**, 828–846.

ATTACHMENT 2: CODE LIST

Table 1: IVM Data Handling and Parametrization IDL Code List[1]

analyze_jjstruc.pro	apply_offset.pro	avg_times.pro
calc_errors.pro	ch_point_info.pro	converttime.pro
cross_correl.pro	csh_jj.pro	cshear_jjstruc.pro
define_jjstruc.pro	derive_seeing.pro	do_analyze_jjstruc.pro
do_divBh.pro	do_fix_analyze_jjstruc.pro	do_paper_plot_params.pro
do_run_plot_params.pro	doublebz.pro	doy.pro
expand_point.pro	extract_date.pro	fixshear.pro
get_img_mm.pro	get_offset.pro	intores.pro
ivm_mdi_align.pro	jjivm_mask.pro	load_analyze.pro
loadofftrim.pro	make_param.pro	mask_pukas.pro
moment_err.pro	moment_weight.pro	my_shift.pro
outofres.pro	paper_plot_icimage.pro	paper_run_plot_params.pro
plot_flare_params.pro	plot_qNd.pro	read_jj_data.pro
read_jjstruc.pro	read_offsets.pro	redoquicklooks.pro
run_plot_params.pro	save_jjtime.pro	save_offsets.pro
see_data.pro	select_data_box.pro	shift_center.pro
startit.pro	test_bperr.pro	time_startstop.pro
timetostring.pro	trim_array.pro	trim_resize.pro
yrdaytodate.pro	zero_entries.pro	

[1] The IVM Data Reduction code is available at:
www.solar.ifa.hawaii.edu/Reference/IVM/IVM_data_red.html

Table 2: Discriminant Function IDL Code List

all_dist.pro	analyze_dfa.pro	count_dfa.pro
dfa.pro	dfa_fake.pro	dfa_fortran.pro
dist_dfa.pro	err_write.pro	inc.pro
mkflarect.pro	sort_dfa.pro	sort_rd.pro
sortp2_dfa.pro		

Table 3: Discriminant Function FORTRAN Code List

programs	subroutines	functions
one_dfa.f	dfa(ivar,x1,ifl1,err)	betacf(a,b,x)
err_dfa.f	ludcmp(a,indx,d)	betai(a,b,x)
sort_dfa.f	lubksb(a,indx,b)	gammln(xx)
	rd_dfa	

1

Table 4: MCT IDL Code List

addmask.pro	advance_diff_rot.pro	all_nulls.pro
all_seprs.pro	allmask.pro	analyze_mct.pro
animate_mask.pro	animate_partition.pro	ar_err_struc.pro
arr2mg.pro	assemble.pro	assemble1.pro
assemble_err.pro	auto_con.pro	auto_mask.pro
auto_maskf.pro	automate.pro	automate1.pro
automatens.pro	avg_bp.pro	bipole.pro
bp_eval.pro	calc_err.pro	clip_fl.pro
closest_pole.pro	colorscale.pro	colorscale2.pro
compare.pro	complete_elliptic_int.pro	connectivity.pro
correct_con.pro	correct_con1.pro	create_null.pro
create_null0.pro	cribbon.pro	crit_stress.pro
ctest.pro	def_region.pro	disk2tan_plane.pro
display.pro	do_paper_plot_params.pro	do_report_plot_params.pro
eigendwl.pro	ell_func_rc.pro	ell_func_rd.pro
ell_func_rf.pro	err_std.pro	err_std0.pro
err_std_struc.pro	err_struc.pro	eval_a.pro
eval_a_ff.pro	eval_b.pro	eval_b2p.pro
eval_b_ff.pro	eval_bprime.pro	eval_bprime_ff.pro
eval_chi.pro	evolve_poles.pro	exp_grid.pro
filter.pro	find_all.pro	find_chrg.pro
find_chrg1.pro	find_chrga.pro	find_null.pro
fl_from_point.pro	fl_from_point0.pro	fl_intgrt.pro
fl_view_xform.pro	fwrite_pns.pro	gamma_line.pro ·
get_berrs.pro	gradient_mask.pro	hel_char.pro
imgexp.pro	imgscl_fen.pro	in_region.pro
init_sepx_line.pro	interp_poles.pro	inv_lam_func.pro
jjtime2pls.pro	kpno_rd.pro	label.pro
length_vector.pro	line_info.pro	line_piece.pro •
line_piece0.pro	locate_sepr.pro	make_mask.pro
mask_file.pro	mct_struc.pro	mdi_rd.pro
merge_nls.pro	merge_nls_label.pro	merge_pls.pro
merge_pls1.pro	merge_pns.pro	mg.pro
mgplot.pro	mkbwt.pro	mkcolort.pro
mkflarect.pro	moment_err.pro	moment_weight.pro
more_nulls.pro	most_nulls.pro	mp.pro
munpack.pro	mut_induct_mat.pro	normalize_3dvec.pro
null_scan.pro	num_pns.pro	old_run_plot_params.pro
one_err.pro	one_err_struc.pro	paper_run_plot_params.pro
par_err.pro	parameter.pro	pb_ang.pro
pixel2tan_plane.pro	plot_flare_params.pro	pls_struc.pro
pns_err_struc.pro	pns_err_struc1.pro	pns_struc.pro
pns_test.pro	pole_crash.pro	post_rx_fl.pro
random_field_line.pro	rd_connect.pro	rd_connects.pro
rd_multi.pro	rd_nulls.pro	rd_pns.pro
rd_poles.pro	rdnls.pro	rdpls.pro
rdsepr.pro	rdview.pro	regchar.pro
region_anl.pro	resolve.pro	run_plot_params.pro

Table 4: – Continued

scale_pls.pro	script.pro	sepr_info.pro
sepr_line.pro	sepr_plane.pro	sepx_line.pro
sepx_pole_map.pro	set_brmax.pro	show_3dnulls.pro
show_3dpoles.pro	show_all.pro	show_all_struc.pro
show_alls.pro	show_alls_err.pro	show_ass.pro
show_con_dev.pro	show_connectivity.pro	show_cr_skel.pro
show_dev.pro	show_domain.pro	show_err.pro
show_flux_dist.pro	show_flux_tube.pro	show_gamma_lines.pro
show_jjtime.pro	show_loop_skeleton.pro	show_mask.pro
show_nulls.pro	show_one_pmap.pro	show_partition.pro
show_plane.pro	show_pns.pro	show_pns_struc.pro
show_pns_struc1.pro	show_poles.pro	show_random_3dlines.pro
show_sepr.pro	show_sepr2.pro	show_sepx.pro
show_spx_xangles.pro	show_z0_fl.pro	solar_rotate_view.pro
spr_polar2xyz.pro	spx_xangles.pro	sun_globe.pro
tan_plane2disk.pro	tan_plane_matrix.pro	test_img.pro
track_multi_null.pro	track_null.pro	triad.pro
update_nulls.pro	upright.pro	vertical_filter.pro
view_xform.pro	write_connect.pro	write_connects.pro
write_err.pro	write_pls.pro	write_pns.pro
xmgp.pro	xmgpart.pro	xselect_nulls.pro
yet_more_nulls.pro		

Table 5: MCT FORTRAN Code List

programs	subroutines	functions
connectivity.f	eulerstep urand_init	intflag ilev cang urand ran2